Real-time eye motion correction in phase-resolved OCT angiography with tracking SLO

Boy Braaf,[1,*] Kari V. Vienola,[1] Christy K. Sheehy,[2] Qiang Yang,[3] Koenraad A. Vermeer,[1] Pavan Tiruveedhula,[2] David W. Arathorn,[3] Austin Roorda,[2] and Johannes F. de Boer[1,4]

[1]*Rotterdam Ophthalmic Institute, Schiedamse Vest 160, 3011 BH Rotterdam, Netherlands*
[2]*School of Optometry, University of California, Berkeley; Berkeley, CA 94720, USA*
[3]*Montana State University, Bozeman, MT 59717, USA*
[4]*LaserLaB, Department of Physics and Astronomy, VU University, de Boelelaan 1081, 1081 HV Amsterdam, Netherlands*
*b.braaf@eyehospital.nl

Abstract: In phase-resolved OCT angiography blood flow is detected from phase changes in between A-scans that are obtained from the same location. In ophthalmology, this technique is vulnerable to eye motion. We address this problem by combining inter-B-scan phase-resolved OCT angiography with real-time eye tracking. A tracking scanning laser ophthalmoscope (TSLO) at 840 nm provided eye tracking functionality and was combined with a phase-stabilized optical frequency domain imaging (OFDI) system at 1040 nm. Real-time eye tracking corrected eye drift and prevented discontinuity artifacts from (micro)saccadic eye motion in OCT angiograms. This improved the OCT spot stability on the retina and consequently reduced the phase-noise, thereby enabling the detection of slower blood flows by extending the inter-B-scan time interval. In addition, eye tracking enabled the easy compounding of multiple data sets from the fovea of a healthy volunteer to create high-quality eye motion artifact-free angiograms. High-quality images are presented of two distinct layers of vasculature in the retina and the dense vasculature of the choroid. Additionally we present, for the first time, a phase-resolved OCT angiogram of the mesh-like network of the choriocapillaris containing typical pore openings.

© 2012 Optical Society of America

OCIS codes: (110.0110) Imaging systems; (170.3880) Medical and biological imaging; (110.4500) Optical coherence tomography; (170.4470) Ophthalmology; (280.2490) Flow diagnostics.

References and links

1. L. A. Yannuzzi, K. T. Rohrer, L. J. Tindel, R. S. Sobel, M. A. Costanza, W. Shields, and E. Zang, "Fluorescein angiography complication survey," Ophthalmology **93**(5), 611–617 (1986).
2. M. Hope-Ross, L. A. Yannuzzi, E. S. Gragoudas, D. R. Guyer, J. S. Slakter, J. A. Sorenson, S. Krupsky, D. A. Orlock, and C. A. Puliafito, "Adverse reactions due to indocyanine green," Ophthalmology **101**(3), 529–533 (1994).
3. D. Huang, E. A. Swanson, C. P. Lin, J. S. Schuman, W. G. Stinson, W. Chang, M. R. Hee, T. Flotte, K. Gregory, C. A. Puliafito, and J. G. Fujimoto, "Optical coherence tomography," Science **254**(5035), 1178–1181 (1991).
4. J. F. de Boer, B. Cense, B. H. Park, M. C. Pierce, G. J. Tearney, and B. E. Bouma, "Improved signal-to-noise ratio in spectral-domain compared with time-domain optical coherence tomography," Opt. Lett. **28**(21), 2067–2069 (2003).
5. R. Leitgeb, C. Hitzenberger, and A. Fercher, "Performance of fourier domain vs. time domain optical coherence tomography," Opt. Express **11**(8), 889–894 (2003).
6. M. Choma, M. Sarunic, C. Yang, and J. Izatt, "Sensitivity advantage of swept source and Fourier domain optical coherence tomography," Opt. Express **11**(18), 2183–2189 (2003).
7. S. Yazdanfar, A. M. Rollins, and J. A. Izatt, "Imaging and velocimetry of the human retinal circulation with color Doppler optical coherence tomography," Opt. Lett. **25**(19), 1448–1450 (2000).

8. B. White, M. Pierce, N. Nassif, B. Cense, B. Park, G. Tearney, B. Bouma, T. Chen, and J. de Boer, "*In vivo* dynamic human retinal blood flow imaging using ultra-high-speed spectral domain optical coherence tomography," Opt. Express **11**(25), 3490–3497 (2003).
9. R. Leitgeb, L. Schmetterer, W. Drexler, A. Fercher, R. Zawadzki, and T. Bajraszewski, "Real-time assessment of retinal blood flow with ultrafast acquisition by color Doppler Fourier domain optical coherence tomography," Opt. Express **11**(23), 3116–3121 (2003).
10. J. A. Izatt, M. D. Kulkarni, S. Yazdanfar, J. K. Barton, and A. J. Welch, "*In vivo* bidirectional color Doppler flow imaging of picoliter blood volumes using optical coherence tomography," Opt. Lett. **22**(18), 1439–1441 (1997).
11. Y. Zhao, Z. Chen, C. Saxer, S. Xiang, J. F. de Boer, and J. S. Nelson, "Phase-resolved optical coherence tomography and optical Doppler tomography for imaging blood flow in human skin with fast scanning speed and high velocity sensitivity," Opt. Lett. **25**(2), 114–116 (2000).
12. R. K. Wang, S. L. Jacques, Z. Ma, S. Hurst, S. R. Hanson, and A. Gruber, "Three dimensional optical angiography," Opt. Express **15**(7), 4083–4097 (2007).
13. B. J. Vakoc, R. M. Lanning, J. A. Tyrrell, T. P. Padera, L. A. Bartlett, T. Stylianopoulos, L. L. Munn, G. J. Tearney, D. Fukumura, R. K. Jain, and B. E. Bouma, "Three-dimensional microscopy of the tumor microenvironment *in vivo* using optical frequency domain imaging," Nat. Med. **15**(10), 1219–1223 (2009).
14. X. J. Wang, T. E. Milner, and J. S. Nelson, "Characterization of fluid flow velocity by optical Doppler tomography," Opt. Lett. **20**(11), 1337–1339 (1995).
15. Z. Chen, T. E. Milner, D. Dave, and J. S. Nelson, "Optical Doppler tomographic imaging of fluid flow velocity in highly scattering media," Opt. Lett. **22**(1), 64–66 (1997).
16. J. Barton and S. Stromski, "Flow measurement without phase information in optical coherence tomography images," Opt. Express **13**(14), 5234–5239 (2005).
17. A. Mariampillai, B. A. Standish, E. H. Moriyama, M. Khurana, N. R. Munce, M. K. Leung, J. Jiang, A. Cable, B. C. Wilson, I. A. Vitkin, and V. X. Yang, "Speckle variance detection of microvasculature using swept-source optical coherence tomography," Opt. Lett. **33**(13), 1530–1532 (2008).
18. J. Fingler, D. Schwartz, C. Yang, and S. E. Fraser, "Mobility and transverse flow visualization using phase variance contrast with spectral domain optical coherence tomography," Opt. Express **15**(20), 12636–12653 (2007).
19. I. Grulkowski, I. Gorczynska, M. Szkulmowski, D. Szlag, A. Szkulmowska, R. A. Leitgeb, A. Kowalczyk, and M. Wojtkowski, "Scanning protocols dedicated to smart velocity ranging in spectral OCT," Opt. Express **17**(26), 23736–23754 (2009).
20. S. Makita, F. Jaillon, M. Yamanari, M. Miura, and Y. Yasuno, "Comprehensive *in vivo* micro-vascular imaging of the human eye by dual-beam-scan Doppler optical coherence angiography," Opt. Express **19**(2), 1271–1283 (2011).
21. S. Zotter, M. Pircher, T. Torzicky, M. Bonesi, E. Götzinger, R. A. Leitgeb, and C. K. Hitzenberger, "Visualization of microvasculature by dual-beam phase-resolved Doppler optical coherence tomography," Opt. Express **19**(2), 1217–1227 (2011).
22. B. Braaf, K. A. Vermeer, K. V. Vienola, and J. F. de Boer, "Angiography of the retina and the choroid with phase-resolved OCT using interval-optimized backstitched B-scans," Opt. Express **20**(18), 20516–20534 (2012).
23. V. X. D. Yang, M. L. Gordon, A. Mok, Y. H. Zhao, Z. P. Chen, R. S. C. Cobbold, B. C. Wilson, and I. A. Vitkin, "Improved phase-resolved optical Doppler tomography using the Kasai velocity estimator and histogram segmentation," Opt. Commun. **208**(4–6), 209–214 (2002).
24. B. Park, M. C. Pierce, B. Cense, S. H. Yun, M. Mujat, G. Tearney, B. Bouma, and J. de Boer, "Real-time fiber-based multi-functional spectral-domain optical coherence tomography at 1.3 microm," Opt. Express **13**(11), 3931–3944 (2005).
25. S. Martinez-Conde, S. L. Macknik, and D. H. Hubel, "The role of fixational eye movements in visual perception," Nat. Rev. Neurosci. **5**(3), 229–240 (2004).
26. S. Ricco, M. Chen, H. Ishikawa, G. Wollstein, and J. Schuman, "Correcting motion artifacts in retinal spectral domain optical coherence tomography via image registration," Med Image Comput Comput Assist Interv **12**(Pt 1), 100–107 (2009).
27. T. Klein, W. Wieser, R. André, T. Pfeiffer, C. M. Eigenwillig, and R. Huber, "Multi-MHz FDML OCT: snapshot retinal imaging at 6.7 million axial-scans per second," Proc. SPIE **8213**, 82131E, 82131E-6 (2012).
28. R. D. Ferguson, D. X. Hammer, L. A. Paunescu, S. Beaton, and J. S. Schuman, "Tracking optical coherence tomography," Opt. Lett. **29**(18), 2139–2141 (2004).
29. R. Ferguson, D. Hammer, A. Elsner, R. Webb, S. Burns, and J. Weiter, "Wide-field retinal hemodynamic imaging with the tracking scanning laser ophthalmoscope," Opt. Express **12**(21), 5198–5208 (2004).
30. D. X. Hammer, R. D. Ferguson, A. H. Patel, V. Vazquez, and D. Husain, "Angiography with a multifunctional line scanning ophthalmoscope," J. Biomed. Opt. **17**(2), 026008 (2012).
31. K. V. Vienola, B. Braaf, C. K. Sheehy, Q. Yang, P. Tiruveedhula, D. W. Arathorn, J. F. de Boer, and A. Roorda, "Real-time eye motion compensation for OCT imaging with tracking SLO," Biomed. Opt. Express **3**(11), 2950–2963 (2012).
32. C. K. Sheehy, Q. Yang, D. W. Arathorn, P. Tiruveedhula, J. F. de Boer, and A. Roorda, "High-speed, image-based eye tracking with a scanning laser ophthalmoscope," Biomed. Opt. Express **3**(10), 2611–2622 (2012).
33. S. Poonja, S. Patel, L. Henry, and A. Roorda, "Dynamic visual stimulus presentation in an adaptive optics scanning laser ophthalmoscope," J. Refract. Surg. **21**(5), S575–S580 (2005).
34. B. Braaf, K. A. Vermeer, V. A. Sicam, E. van Zeeburg, J. C. van Meurs, and J. F. de Boer, "Phase-stabilized optical frequency domain imaging at 1-μm for the measurement of blood flow in the human choroid," Opt. Express **19**(21), 20886–20903 (2011).

35. Q. Yang, D. W. Arathorn, P. Tiruveedhula, C. R. Vogel, and A. Roorda, "Design of an integrated hardware interface for AOSLO image capture and cone-targeted stimulus delivery," Opt. Express **18**(17), 17841–17858 (2010).
36. S. Makita, Y. Hong, M. Yamanari, T. Yatagai, and Y. Yasuno, "Optical coherence angiography," Opt. Express **14**(17), 7821–7840 (2006).
37. M. H. Bernstein and M. J. Hollenberg, "Fine structure of the choriocappillaris and retinal capillaries," Invest. Ophthalmol. **4**(6), 1016–1025 (1965).
38. F. Jaillon, S. Makita, and Y. Yasuno, "Variable velocity range imaging of the choroid with dual-beam optical coherence angiography," Opt. Express **20**(1), 385–396 (2012).
39. S. Yoneya and M. O. Tso, "Angioarchitecture of the human choroid," Arch. Ophthalmol. **105**(5), 681–687 (1987).
40. A. W. Fryczkowski and M. D. Sherman, "Scanning electron microscopy of human ocular vascular casts: the submacular choriocapillaris," Acta Anat. (Basel) **132**(4), 265–269 (1988).
41. J. M. Olver, "Functional anatomy of the choroidal circulation: methyl methacrylate casting of human choroid," Eye (Lond.) **4**(2), 262–272 (1990).
42. ANSI, "American National Standard for the Safe use of Lasers," ANSI Z136.1 (Laser Institute of America, Orlando, FL, 2007).
43. F. C. Delori, R. H. Webb, and D. H. Sliney, "Maximum permissible exposures for ocular safety (ANSI 2000), with emphasis on ophthalmic devices," J. Opt. Soc. Am. A **24**(5), 1250–1265 (2007).

1. Introduction and theory

Angiography is routinely used in ophthalmology for the assessment of the retinal and choroidal circulation and has become essential in the diagnosis of ocular pathology. Current established tools for ophthalmic angiography are fluorescein angiography (FA) and indocyanine green angiography (ICGA). In both methods a dye is injected intravenously to obtain photos of the circulation with high contrast. Unfortunately, adverse reactions to these dyes do occur [1,2]. A non-invasive imaging method is therefore preferable for frequent follow-up measurements and the screening of large populations.

The introduction of optical coherence tomography (OCT) has revolutionized ophthalmology by providing non-invasive cross-sectional imaging of retinal and choroidal structures with high axial (2-15 µm) and lateral (5-30 µm) resolutions [3]. Especially the improved detection sensitivity and acquisition speed of Fourier-domain OCT has made OCT suitable for clinical investigations [4–6]. In the past two decades several angiographic imaging extensions have been developed for OCT to complement or potentially replace existing angiography techniques for investigations of *in vivo* vascular networks of e.g. the eye [7–9], the skin [10,11], the brain [12], and in microscopy applications on *in vitro* tissues [13]. In OCT angiography blood flow is discriminated from static tissues by analyzing phase changes [11,12,14,15] or intensity changes [16,17] in the OCT signal that are caused by moving light-scattering particles. In ophthalmology inter-B-scan phase-resolved (Doppler) OCT has been successfully shown for the imaging of blood flow in the (micro-)vasculature of the retina and choroid [18–22].

In phase-resolved OCT blood flow is detected from the phase-difference $\Delta\phi$ between two A-scans [11]:

$$\Delta\phi = \frac{4\pi n\tau v_{flow}}{\lambda_0}\cos(\alpha), \tag{1}$$

in which n is the refractive index of the tissue, τ is the time interval between the two A-scans, v_{flow} is the blood flow velocity, λ_0 is the center wavelength of the OCT light source, and α is the angle between the flow velocity direction and the OCT-beam which is also known as the Doppler angle. The noise on the phase-difference, the phase-noise $\sigma_{\Delta\phi}$, defines the smallest observable phase-difference and therefore the minimum detectable flow velocity is given by: $v_{min} = (\sigma_{\Delta\phi}\cdot\lambda_0)/(4\pi n\tau\cdot\cos(\alpha))$ [9,23]. The phase-noise follows a Gaussian probability distribution, for which $\sigma_{\Delta\phi}$ represents the standard deviation, and depends on the signal-to-noise ratio (SNR) and on noise caused by an imperfect spot overlap between the compared A-scans [24]:

$$\sigma_{\Delta\phi} = \sqrt{\left(\frac{1}{SNR_s}\right) + \left(\frac{4\pi}{3}\right)\left(1 - \exp\left(-2\left(\frac{\Delta x}{d}\right)^2\right)\right)}. \qquad (2)$$

In Eq. (2) SNR_s is the ratio of the OCT sample signal strength and the mean noise floor, d is the spot diameter of the focused OCT-beam on the sample, and Δx is the spot displacement between the two A-scans. A high phase-noise due to a low SNR_s or a high $\Delta x/d$ ratio results in a high v_{min} and makes the detection of blood flow more difficult. This restricts any spot displacement to be within a small fraction of the spot size for good quality angiograms. In phase-resolved OCT spot diameters around 10 to 30 µm are commonly used and the spot displacement that is allowed is therefore limited to a few microns. Consequently, phase-resolved OCT is vulnerable to eye motion which creates artifacts and increased noise levels, especially when a large time interval τ is used [21,22].

Involuntary fixational eye motion (e.g. drift and microsaccades [25]) is a major cause of artifacts in OCT imaging [26] even in ultra-high speed systems [27]. Currently, several commercial OCT instruments therefore include auxiliary hardware to measure and correct eye motion in real-time e.g. Spectralis OCT (Heidelberg Engineering, Heidelberg, Germany), RTVue (Optovue Inc., CA, USA) and tracking OCT from Physical Sciences Inc. (PSI) [28]. In these systems the retinal motion is extracted from temporal changes in either scanning laser ophthalmoscope (SLO) images (Spectralis OCT), full-field fundus images (RTVue) or the reflectance of single retinal features (PSI). All three systems use the measured eye motion to lock the OCT scanning grid on its moving retinal target by either direct correction of the OCT galvanometer scanners or correction via secondary tracking scanners. In respect to angiography, only the PSI tracking technology was shown for the purpose of stabilizing SLO based laser Doppler flowmetry [29] and FA/ICGA imaging [30].

In this paper we present eye-motion-corrected inter-B-scan phase-resolved OCT angiography using a phase-stabilized optical frequency domain imaging (OFDI) system combined with experimental real-time tracking SLO (TSLO). It was shown previously that the combined OFDI-TSLO setup was able to significantly reduce the amount of eye motion artifacts in OCT intensity imaging of retinal structures and the optic nerve head [31]. Using this setup we show, to our knowledge, for the first time how eye tracking reduces artifacts in phase-resolved OCT angiograms and analyze its performance with respect to the spot stability on the retina. Further, we show that eye tracking enables the compounding of multiple 3D data sets from the same location to produce high-quality eye motion artifact-free angiograms of the fovea of a healthy volunteer. High-quality images are presented of two distinct layers of vasculature in the retina, the dense vasculature of the choroid, and the mesh-like network of the choriocapillaris.

2. Experimental system description

The optical layout of the OFDI-TSLO setup is shown in Fig. 1 and the specifications of the individual OFDI and TSLO setups, as well as the combined operation, are summarized below.

2.1. Tracking scanning laser ophthalmoscope setup

The TSLO setup was described previously by Sheehy et al. [32] and was specifically designed for high-speed image-based tracking of retinal motion. It was used in this study to image the retina over a 4° field-of-view and its optical paths are shown in Fig. 1 in blue. An 840 nm super luminescent diode (SLD) was used as the light source and provided an optical power of 0.5 mW on the cornea. The system contains three large telescopes composed of curved mirrors to accurately image two scan mirrors for horizontal (HS) and vertical (VS) scanning to the pupil of the eye. A beam splitter (BS) was used to relay returning light to a photo-multiplier tube (PMT) for detection. A pinhole (P) was placed in front of the PMT to provide confocal imaging. Two diaphragms (D) were used to control the input beam size and to block light scattered within the setup from entering the PMT. An acoustic optical modulator (AOM) was connected to the SLD to limit the light exposure by blocking the light during the scanner

fly-back. The AOM also provides a fixation target to the subject by blocking the light for a specific part of the field-of-view [33]. This creates a dark fixation dot against an illuminated background which was used for alignment of the subject. The TSLO images the retina with 512 x 512 pixel frames acquired at a 30 Hz frame rate.
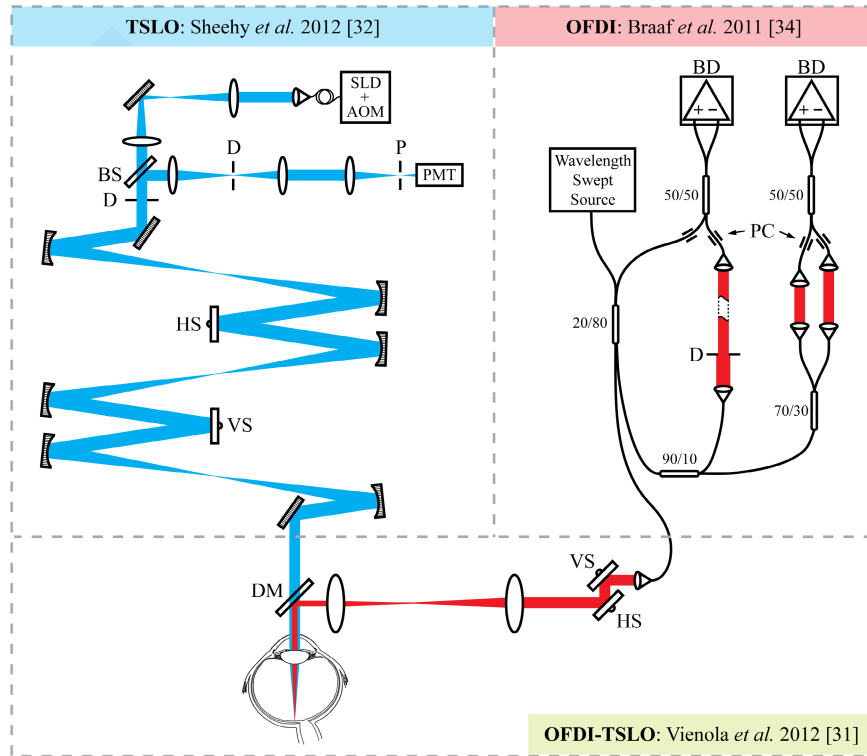

Fig. 1. The optical layout of the combined OFDI-TSLO setup. (TSLO PANEL) The TSLO schematic with its optical paths in blue. A super luminescent diode (SLD) was used as the light-source combined with an acoustic-optic modulator (AOM). The light is directed via a set of lenses to three curved mirror telescopes to image a horizontal scanner (HS) and a vertical scanner (VS) onto the pupil of the eye. A beam splitter (BS) was used to relay returning light to a photo-multiplier tube (PMT) for detection. A pinhole (P) is used to provide confocal retinal imaging and two diaphragms (D) are used to control the input beam size on the eye and to block light scattered within the setup from the PMT. (OFDI PANEL) The OFDI schematic with its optical paths in red. Light from a wavelength swept-source is passed on into a fiber-based interferometer that splits into a sample arm to the eye and a reference arm. Scattered light from the eye is recombined with the reference arm light at a 50/50 coupler and detected with balanced detection (BD). An additional Mach-Zehnder interferometer is attached to the reference arm with a 90/10 coupler to simultaneously measure a calibration signal and forms the second interferometer channel. Interferometric detection was optimized using in-line polarization controllers (PC). (OFDI-TSLO PANEL) The TSLO and the OFDI were coupled together via a dichroic mirror (DM).

2.2. Phase-stabilized optical frequency domain imaging setup

The OFDI setup used in this study was described previously by our group [34] and its optical paths are shown in Fig. 1 in red. In summary the setup uses a 1-µm swept-source with a fixed repetition rate of 100 kHz (Axsun technologies) and a fiber-based interferometer which provided an axial resolution of 4.8 µm (6.5 µm in air). Careful adjustment of the reference arm power with a diaphragm (D) and the use of balanced detection (BD) enabled a system operation < 1 dB from the shot-noise. In order to calibrate and phase-stabilize the OCT measurements, a parallel Mach-Zehnder interferometer (MZI) was embedded in the setup to map A-scan spectra to the same wavenumbers (k-space). This enabled the suppression of

fixed-pattern noise and phase-artifacts to negligible levels [34]. The MZI is shown as the right interferometer channel connected to the 90/10 fiber-coupler in Fig. 1. The OFDI sample arm consisted of a pair of galvanometer scanners (Thorlabs GVS002) for vertical (VS) and horizontal (HS) scanning and a demagnifying telescope. A dichroic mirror (DM) was used to couple the OFDI together with the TSLO. In this study the beam diameter ($1/e^2$) on the cornea was 1.2 mm which gave a theoretical diffraction limited retinal spot-size of 18.6 µm. The optical power was 1.5 mW for which a sensitivity of 101.9 dB was measured on a mirror.

2.3. Real-time eye tracking and simultaneous OFDI-TSLO operation

The eye motion was extracted from the TSLO images in real-time as described by Yang *et al.* [35] and Sheehy *et al.* [32]. In brief, a TSLO frame is selected by the operator to serve as a reference. Consecutive TSLO frames are broken down into small horizontal strips which are cross-correlated one by one with the reference frame. The displacement of each strip with respect to its reference location provides the eye motion. In this study each TSLO frame was broken down into 32 overlapping strips of 32 pixels in height and 512 pixels in width to report the eye motion at 960 Hz [31,32].

The reported eye motion was inverted, converted into a voltage signal, and added to the waveforms that drive the OFDI galvanometer scanners to correct for lateral retinal motion. Additionally, the TSLO signaled the OFDI with a validity signal in case of tracking failures, e.g. caused by large saccades or blinks, to mark B-scans that were distorted by eye motion as invalid. These B-scans were immediately reacquired and the distorted versions of these B-scans were removed in post-processing to obtain a motion-free OCT data volume. The combined OFDI-TSLO setup achieved a 3 dB motion correction bandwidth of 32 Hz and a B-scan stability accuracy of 1.6 µm (0.32 arcmin) along the fast-axis scanning direction. A detailed technical description and the performance analysis on the simultaneous OFDI-TSLO operation can be found in Vienola *et al.* [31]. Laser safety considerations for the simultaneous OFDI-TSLO operation can be found in the Appendix A of the current paper.

Vienola *et al.* described that distortions in the TSLO reference frame and torsion of the eye gives rise to periodic motion artifacts in the eye motion correction at the 30 Hz TSLO frame rate [31]. In the course of this study, it was found that this affected the OCT spot stability and therefore the imaging quality. As a solution we low-pass filtered the motion correction signals at a 10 Hz cutoff frequency with a low-noise preamplifier (Stanford Research Systems SR560) before addition to the galvanometer waveforms. Although this reduced the motion correction bandwidth to 10 Hz, it had a minimal effect on the overall system performance since the eye motion amplitude at frequencies above 10 Hz is generally less than 2.5 µm (0.5 arcmin) as was reported by Sheehy *et al.* [32].

2.4. Inter-B-scan phase-resolved OCT imaging protocol and post-processing

In this study inter-B-scan phase-resolved OCT imaging was performed by acquiring two B-scans at the same retinal location with a saw-tooth waveform. A single B-scan consisted of 1000 A-scans, including 200 A-scans for galvanometer scanner fly-back. This provided a 10 ms phase-resolved imaging time interval for which a phase-noise of 0.44 ± 0.13 rad was measured with eye tracking (details in Subsection 3.1). Using Eq. (1) the corresponding minimal flow velocity that can be observed was calculated as 0.15 ± 0.04 mm/s for a Doppler angle of 89°. This should reveal the slowest blood flow that can be found in the retinal capillaries and the choriocapillaris, which ranges from 0.2 to 3.6 mm/s [22]. The images presented in Subsection 3.2 and thereafter are acquired with a scan-grid consisting of 300 vertically oriented B-scan locations covering a retinal surface area of 2.0 x 2.0 mm^2. The total acquisition time for a single data set ranged from 6.0 to 6.5 s depending on the amount of invalid B-scans.

Axial sample motion was corrected using the two-step correction algorithm from our previous study [22]. First, large axial displacements were estimated with cross-correlation from the axial (sub-)pixel shift in between the intensity images of the compared B-scans. The found shift in pixels, Δp, was corrected by multiplication of the OCT signals $S_{oct}(k)$ of the

second B-scan with a complex exponential function: $\tilde{S}_{oct}(k) = S_{oct}(k) \cdot \exp(-i\,2\pi\,k\,\Delta p)$.
Afterwards, any remaining axial displacement was corrected using histogram-based normalization similar as described by Makita *et al.* [36].

Finally, the inter-B-scan phase-differences were calculated by subtraction of the phase information for each set of B-scans. Similar to our previous study, locations with blood flow were determined by calculation of the absolute phase-difference and were emphasized by median filtering and thresholds on intensity (10 dB) and absolute phase-difference (0.4 rad) [22]. Subsequently, en face angiograms were created by integration of the flow information over depth.

2.5. Ethical considerations

The use of our experimental setup for *in vivo* measurements in humans was approved by the local Institutional Review Board and adhered to the tenets of the Declaration of Helsinki. Informed consent was obtained from each subject.

3. The advantages of eye tracking for phase-resolved OCT angiography

In this section we show how eye tracking improves phase-resolved OCT angiography. A performance analysis is presented on the retinal spot stability with and without eye tracking (Subsection 3.1). Further, several examples are provided which illustrate eye motion distortions in an untracked retinal angiogram, the minimization of these artifacts with eye tracking, and the correction of tracking failures caused by saccades (Subsection 3.2).

3.1. Retinal spot stability

In a previous study we showed how the phase-noise in phase-resolved OCT measurements increases over time due to lateral sample motion [22]. This analysis was used to optimize the time interval τ for the imaging of capillary blood flow. In this section the same analysis is used to evaluate the location stability improvement by eye tracking.

The location stability for phase-resolved OCT measurements was determined by imaging the retina of a healthy volunteer without scanning the OCT-beam. During the measurement the subject was asked to look at the fixation target as is done during regular OCT-imaging. 10,000 A-scans were acquired and phase-difference values were calculated by subtracting a time-shifted version of the data from the original data. The amount of time-shifting was varied to obtain phase-differences at different time intervals up to 20 ms. The phase-noise was determined by the standard deviation of the phase-difference values. Artifacts due to blood flow were avoided by using data from the retinal pigment epithelium (RPE) tissue layer near the fovea, where blood vessel shadows are minimal. Subsequently, the spot displacement was calculated using Eq. (2) from the phase-noise and the measured SNR of the RPE tissue layer. Data sets distorted by microsaccades were omitted from the analysis, since these distortions were also removed in the final angiograms (Section 4). The analysis was performed *with* and *without* eye tracking and the mean ± the standard deviation over 10 data sets is reported. An example of a single measurement is displayed in Fig. 2(A) which shows the OCT intensity image (top image) and the phase-difference image (bottom image). The RPE data used in the analysis is indicated by a yellow box.

The spot displacement results are given in Fig. 2(B) in blue solid dots *without* eye tracking and in red open dots *with* eye tracking. The phase-noise is indicated by the secondary y-axis at the right side of the plot. It can be seen that the spot displacement increases over time similarly to our previous study [22]. It is evident from this figure that eye tracking improves the spot stability since the spot displacement *with* eye tracking is smaller than *without* eye tracking for the whole time interval range. Indeed, a two-way ANOVA test confirmed that the overall difference between the two curves is statistically significant with p < 0.001. The improvement increases with longer time intervals and the corresponding reduction in the phase-noise leads to higher quality phase-resolved OCT images. More important, the improved stability *with* eye tracking can be used to extend the time interval for the detection

of slower blood flows without concessions on the phase-noise. In this study, angiograms were measured with an inter-B-scan time interval of 10 ms for which the spot displacement improved from 3.5 ± 0.79 μm (0.55 ± 0.12 rad) *without* eye tracking to 2.8 ± 0.84 μm (0.44 ± 0.13 rad) *with* eye tracking. The improvement of 0.71 μm (0.11 rad) reduced the phase-noise to a level that is equal to the phase-noise *without* eye tracking at 4.2 ms. The 2.4 times longer time interval *with* eye tracking enables the detection of 2.4 times slower blood flows. The improvement factor increased up to 3.3 for a time interval of 20 ms.

The current analysis evaluates the spot stability within the two lateral dimensions simultaneously in contrast to the one-dimensional B-scan stability analysis of Vienola *et al.* [31]. Considering an equal spot stability in both lateral directions, the one dimensional stability performance of Vienola *et al.* [31] (1.6 μm for a 20 ms time interval) can be converted into 2.3 μm for two dimensions by vector addition. The analysis presented in this paper reports a stability of 3.2 ± 0.88 μm at 20 ms. The difference is attributed to a more sensitive detection of spot displacement with phase-noise measurements (this study) compared to the measurement of lateral shifts in between OCT intensity B-scans (Vienola *et al.* [31]), and the inclusion of residual axial motion in the spot displacement in this study.
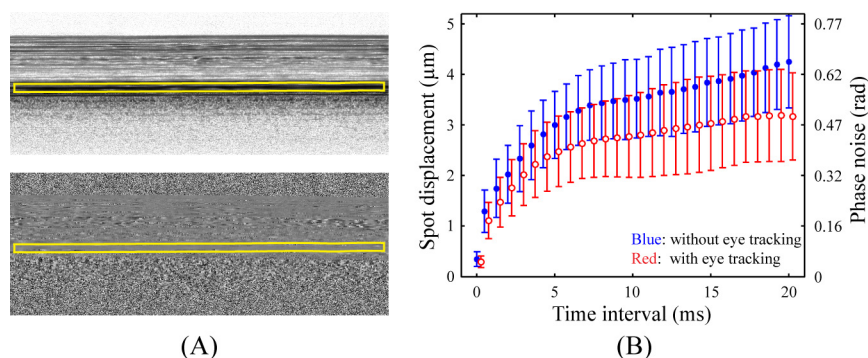

(A)   (B)

Fig. 2. *In vivo* phase-noise measurement due to sample motion. (A) The OCT galvanometer scanners were stopped and A-scans were acquired for a period of 0.1s (10,000 A-scans). The top figure shows the intensity image, the bottom figure shows the phase-difference image for a time interval of 1.0 ms (100 A-scans). The phase-noise was analyzed from the RPE layer (yellow box) to avoid interference with blood flow. (B) The spot displacement due to lateral sample motion *without* eye tracking in blue solid dots and *with* eye tracking in red open dots. To improve the visibility of individual data points the results *with* eye tracking are slightly shifted to the right.

3.2. Correction and removal of image distortions

It has been reported in previous studies that eye motion can create severe artifacts in phase-resolved OCT imaging at long time intervals [21,22]. This is illustrated in Fig. 3 which shows examples of angiograms of the retinal vasculature of the fovea of a healthy volunteer acquired under different imaging conditions.

In Fig. 3(A) a retinal angiogram is shown which was acquired *without* eye tracking. The eye motion measured by the TSLO is shown in the graph below the angiogram with horizontal and vertical eye position plotted respectively in blue and red. Abrupt jumps in the eye position caused by microsaccades create white vertical line artifacts in the angiograms. These line artifacts are caused by the decorrelation of the two B-scans which were not acquired at the exact same location. Further, microsaccades create discontinuities in the angiograms for which several examples are highlighted with yellow boxes. These discontinuities are often accompanied by either a repetition in, or a loss of, a part of the vascular network depending on the direction of the microsaccade. In the latter case, these losses preclude the creation of high quality angiograms. Position changes of the eye due to drift are harder to identify from individual angiograms, but are equally problematic. The eye drift is clearly present in the eye motion graph which shows slow variations in the position over time. Drift is responsible for

displacements and shearing of the angiogram which corrupts the fidelity of the spatial position of the vasculature. Without correction these drifts preclude direct comparisons, overlaying or compounding of angiograms.

(A) Untracked

(B) Tracked

(C) Tracked
Invalid B-scans rescanned

(D) Tracked
Invalid B-scans removed

The TSLO triggers the OFDI in case of tracking failures to rescan areas corrupted by saccades. Invalid B-scans were removed in post-processing.
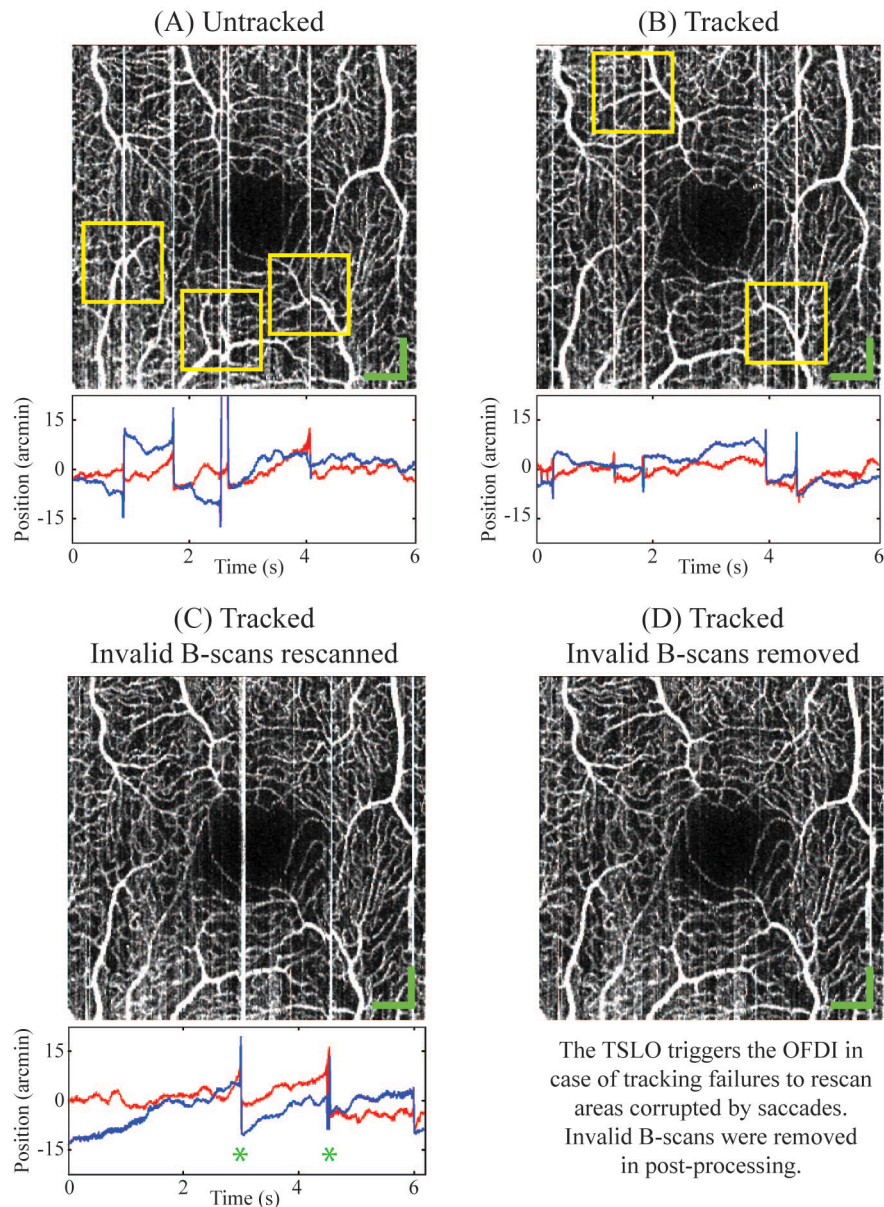
Fig. 3. Examples of eye motion artifacts in phase-resolved OCT angiography of the retina and its correction by eye tracking. The horizontal and vertical eye position are plotted below the angiograms respectively in blue and red. The angiograms display a surface area of 2.0 x 2.0 mm^2. The green scale-bars are 250 µm in length. (A) Untracked. The angiogram is corrupted by microsaccades which create discontinuity artifacts in the visualized vasculature (examples are highlighted by yellow boxes) and white line artifacts. (B) Tracked. The angiogram still shows the line artifacts but the discontinuity artifacts are absent (examples are highlighted by yellow boxes). (C) Tracked + Invalid B-scans rescanned. The TSLO is able to detect untracked (micro)saccades (marked by * in the eye position graph) and signaled the OFDI to reacquire the B-scans during these events. This angiogram includes the corrupted B-scans. (D) Tracked + Invalid B-scans removed. In post-processing the corrupted B-scans were removed. A single undetected artifact remained at the right side.

In Fig. 3(B) an angiogram is shown that was acquired *with* eye tracking. In this case microsaccades cause no or minimal discontinuity artifacts in the vasculature for which several examples are highlighted with yellow boxes. Although the eye tracking corrected drift, it did not completely cancel out saccadic motion and white line artifacts were still created.

Figure 3(C) shows an angiogram taken with eye tracking including the validity signal. Three (micro)saccades occurred during acquisition of which two were detected by the TSLO (marked with asterisks (*) in the eye position graphs). The TSLO signaled the OFDI in real-time during these events to indicate that the currently acquired B-scan is corrupted by saccadic motion. Such a B-scan was then immediately reacquired. In post-processing the motion corrupted version of the B-scan was removed to create an angiogram without discontinuity artifacts as shown in Fig. 3(D). This example shows that in case the actual eye motion could not be tracked, the majority of these artifacts could still be corrected.

4. High-quality eye motion artifact-free phase-resolved OCT angiography

4.1. Segmentation of various vasculature types

In order to appreciate the ability of phase-resolved OCT angiography to detect blood flow within the various vasculature types of the human retina and choroid, image segmentation was applied to the data set of Fig. 3(D). The segmentation was based on the detection of the highest gradient magnitude in OCT intensity B-scans for specific tissue interfaces (edges). In Fig. 4(A) an example is shown of an intensity B-scan with its segmented interfaces. In

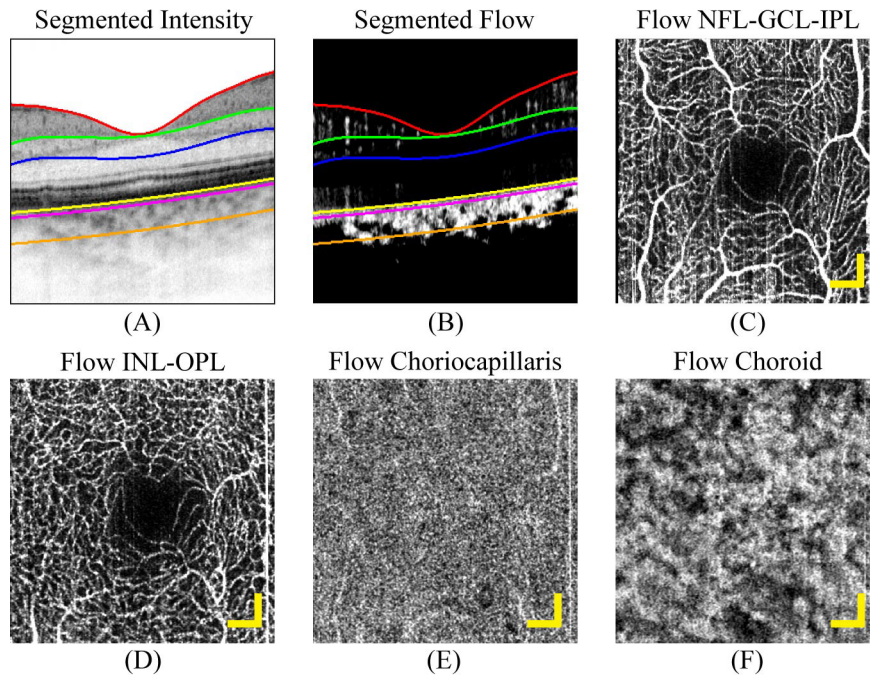| Segmented Intensity	Segmented Flow	Flow NFL-GCL-IPL
(A)	(B)	(C)
Flow INL-OPL	Flow Choriocapillaris	Flow Choroid
(D)	(E)	(F)

Fig. 4. (A) The segmentation of layers with different vascular networks in an OCT intensity B-scan. The first retinal layer (red - green) consists of the nerve fiber layer (NFL), the ganglion cell layer (GCL) and the inner plexiform layer (IPL). The second retinal layer is a 73 μm thick layer below the IPL (green - blue) that consists of the inner nuclear layer (INL) and the outer plexiform layer (OPL). The choriocapillaris is segmented as a 18 μm thick layer below the RPE (yellow - magenta) and the choroid is segmented as a 90 μm thick layer below the choriocapillaris (magenta - orange). (B) The segmentation boundaries overlayed on a flow B-scan. Blood flow is shown as white signals against a black background. (C) Angiogram of the first retinal layer NFL-GCL-IPL. (D) Angiogram of the second retinal layer INL-OPL. (E) Angiogram of the choriocapillaris. (F) Angiogram of the choroid. The angiograms display a surface area of 2.0 x 2.0 mm². The yellow scale-bars are 250 μm in length.

Fig. 4(B) the segmentation interfaces are plotted on top of the corresponding flow B-scan, which shows blood flow as white signals against a black background.

In the retina, two layers of vasculature were considered since a superficial as well as a deeper layer of capillaries have been reported by histological studies [37]. The first layer holds the larger retinal vessels and incorporates the nerve fiber layer (NFL), the ganglion cell layer (GCL), and the inner plexiform layer (IPL). This layer is outlined by the vitreous-NFL interface as plotted in red, and the interface between the IPL and the inner nuclear layer (INL) plotted in green. The second layer incorporates the vasculature within the INL and the outer plexiform layer (OPL) and was segmented by extending the IPL-INL interface with a 73 µm thick layer for which the lower boundary is plotted in blue.

Below the retina two additional layers of vasculature were considered. The choriocapillaris was selected with an 18 µm thick layer below the RPE. This layer is outlined by yellow and magenta segmentation lines. Underneath the choriocapillaris a 90 µm thick layer was segmented to obtain the vasculature of the choroid. Its lower boundary is plotted in orange.

An en face angiogram was created for each layer by integration of the flow signals over depth. Figure 4(C) shows the angiogram of the NFL-GCL-IPL layer in which the superficial vasculature is nicely visualized. The INL-OPL layer in Fig. 4(D) shows additional finer vasculature, but the interpretation is hard due to apparent similarities with the NFL-GCL-IPL layer. These are caused by over-crossing capillaries that connect both layers and Doppler noise shadows that are cast from above. The foveal avascular zone is clearly observed in Figs. 4(C) and 4(D) as the "empty" space in the center of the angiograms. In Fig. 4(E) the uniform layer of flow of the choriocapillaris is shown. The limited thickness of this layer limits a nice visualization but a fine mesh-like structure seems to emerge. The blood flow of the choroid is given in Fig. 4(F) and shows a dense network of large vessels similar as observed in previous studies [22,38].

4.2. High-quality artifact-free angiography by data set compounding

In order to improve the overall quality of the angiograms eight three-dimensional phase-resolved OCT data sets of the fovea were compounded together. Each data set used a new TSLO reference frame to guarantee optimal eye tracking. The slightly varying lateral position of each data set was corrected by image registration. A retinal angiogram was extracted from each data set, from which one was used as a reference to register the other data sets on. This provided the lateral translation and rotation for each data set to exactly overlay all data sets. Eye tracking was essential for this step since eye drift and microsaccades would otherwise give unique distortions in each data set and prevent accurate registration and overlaying. Axial displacements between the data sets were measured by cross-correlation of the OCT intensity B-scans and corrected by axial shifting. Finally, the median value over all eight data sets was taken for every pixel in the volume.

In Fig. 5 high quality angiograms are presented for the retinal vasculature. The individual vessels in the NFL-GCL-IPL layer are very clearly observed in Fig. 5(A) and the noise significantly reduced compared to Fig. 4(C). Additionally, the saccadic artifact at the right of Fig. 4(C) was removed by the median pixel selection. The result is an angiogram which is completely free from eye motion artifacts. Similarly, the visualization of the INL-OPL vasculature is greatly improved in Fig. 5(B) compared to Fig. 4(D) and now shows clearly a different vascular network compared to the NFL-GCL-IPL layer. In addition, the data set compounding significantly reduced the Doppler noise shadow artifacts in the INL-OPL angiogram. A three-dimensional rendering of the entire retinal vasculature is provided in Fig. 5(C) and a link to a movie of the rotating 3D vasculature is provided in the caption. This movie shows how the retinal vasculature is oriented in depth and gives a better view on the axial relation between the two capillary layers than the 2D angiograms.
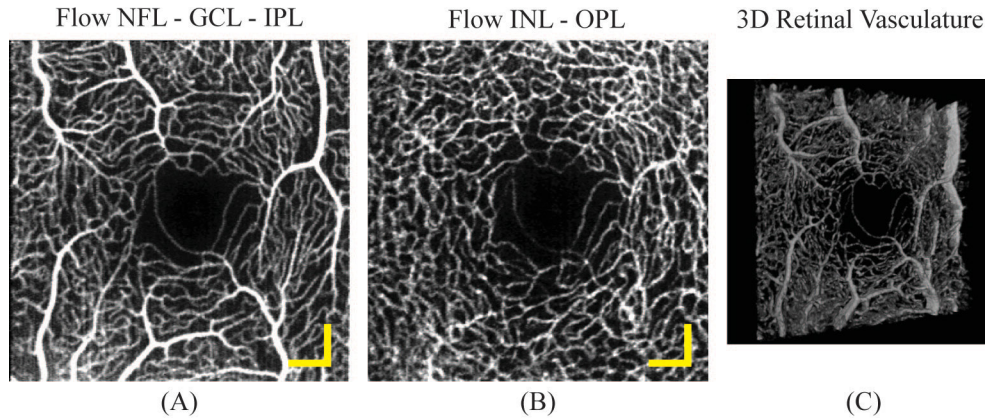
Flow NFL - GCL - IPL   Flow INL - OPL   3D Retinal Vasculature

(A)   (B)   (C)

Fig. 5. High-quality artifact-free angiograms of the retina by compounding eight data sets from the same location with a surface area of 2.0 x 2.0 mm^2. The yellow scale-bars are 250 μm in length. (A) Angiogram of the NFL-GCL-IPL layer clearly showing the vasculature around the foveal avascular zone. (B) Angiogram of the INL-OPL layer showing a fine vascular network. (C) Three-dimensional rendering of the entire retinal vasculature to visualize its orientation in depth. The three-dimensional rendering is also available in a movie: high-resolution (Media 1) and low-resolution (Media 2).

High quality angiograms of the choroid and the choriocapillaris are provided in Fig. 6. The choroidal vasculature in Fig. 6(A) is improved in quality to Fig. 4(F) and shows a dense vascular network right below the fovea. The absence of an orderly choroidal network in the macula has been reported before by scanning electron microscopy studies which described the vessel arrangement as tortuous and intertwined [39]. In the literature the submacular choriocapillaris is described as a monolayer vascular network with a lobular (mesh-like) arrangement [39,40]. The size of the pores in the mesh-like network are known to range in between 5 to 40 μm [40,41]. In the angiogram of Fig. 6(B) the choriocapillaris indeed shows a fine mesh-like network with small black pores where blood flow is absent. Shadows from the larger retinal vessels are cast into this angiogram as large white vessels. A 410 x 410 μm^2 area of the choriocapillaris angiogram, marked by a yellow box in Fig. 6(B), is shown magnified in Fig. 6(C). Several pores are indicated in this magnification by white arrows. The pores have cross-sectional diameters ranging from 20 to 30 μm. These diameters are in good agreement with the largest intercapillary spaces that were reported for the submacular choriocapillaris with scanning electron microscopy [40,41]. Smaller pores are not observed since they exceed the lateral resolution of the system which is currently 18.6 μm. In Fig. 6(D) an example is shown of a scanning electron microscopy image from an *ex vivo* human ocular vascular cast, which is adapted from Olver *et al.* [41]. The choriocapillaris microstructures are marked with a dashed orange box in this image; outside the box remnants of the retinal vasculature are seen. The similarities between the phase-resolved OCT angiogram of the choriocapillaris and the scanning electron microscopy image make it evident that Fig. 6(B) indeed shows choriocapillaris blood flow. In addition, a red square marks a 410 x 410 μm^2 area which is shown magnified in Fig. 6(E). In this image several of the larger choriocapillaris pores are marked with white arrows to indicate pores with a similar size as those observed in Fig. 6(C).

Flow Choroid	Flow Choriocapillaris	Magnified Flow Choriocapillaris
(A)	(B)	(C)

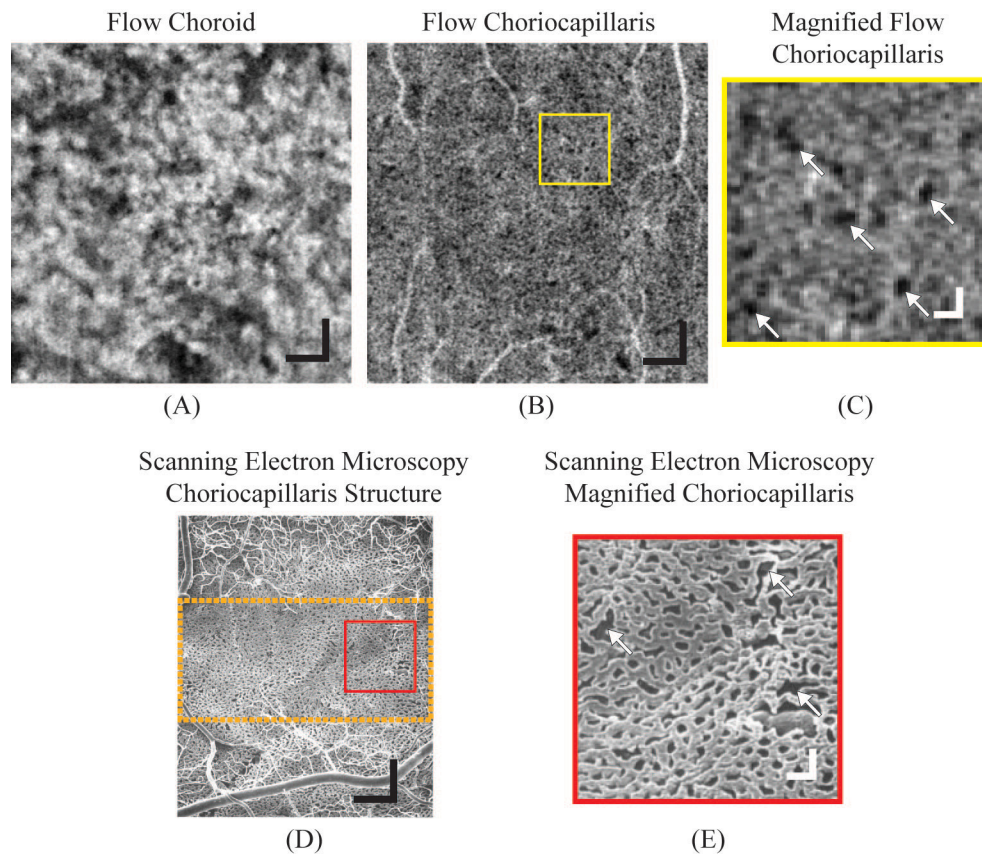| Scanning Electron Microscopy Choriocapillaris Structure	Scanning Electron Microscopy Magnified Choriocapillaris
(D)	(E)

Fig. 6. High-quality artifact-free angiograms of the choroid and the choriocapillaris by compounding eight data sets from the same location. The black scale-bars are 250 µm in length, the white scale-bars are 40 µm in length. (A) *In vivo* angiogram of the choroid showing a dense network of large vessels below the choriocapillaris for a 2.0 x 2.0 mm² area. (B) *In vivo* angiogram of the choriocapillaris showing a mesh-like network of small vessels with small black pores for a 2.0 x 2.0 mm² area. (C) A magnified view on a 410 x 410 µm² area of the choriocapillaris angiogram (marked yellow in (B)) which shows individual pores in detail from which five examples are indicated with white arrows. (D) *Ex vivo* scanning electron microscopy image from a methyl methacrylate cast of an excised eye which shows the subfoveal choriocapillaris microstructures in high-resolution for a 1.8 x 1.5 mm² area. The choriocapillaris structures are marked by an orange box; remnants of the retinal vasculature are seen outside the box. The choriocapillaris angiogram of (B) greatly resembles the microstructures shown in this image. The image was reproduced and adapted from Olver *et al.* [41] with the permission of the Nature Publishing Group. (E) A magnified view from (D) for a 410 x 410 µm² area (marked red in (D)) in which white arrows indicate pores with a similar size as those observed in (C).

5. Discussion

The implementation of eye tracking with TSLO in phase-resolved OCT angiography offers several advantages. It allows one to increase the inter-B-scan time interval for the detection of slower blood flow. Discontinuities and distortions are removed from angiograms through a combination of tracking and careful logging of tracking failures. Consequently, it allows simple compounding of multiple volumes to obtain high quality data. However, the full potential has not been reached for two reasons. First, the TSLO motion correction signal required a 10 Hz low-pass filter to eliminate the 30 Hz motion artifacts that are inherent to the TSLO method [31]. Solving this artifact in future TSLO implementations will enable larger motion correction bandwidths and consequently a better reduction of the phase noise than

reported in this paper. Second, not all saccadic artifacts were detected. Currently the identification of untracked saccades by the TSLO is based on sub threshold correlation values in the strip-based eye motion extraction [31]. One way of making this method more sensitive in the future is to combine it with the detection of abrupt jumps in the eye position, which occurs during saccadic motion.

It was shown in this paper that eye tracking, combined with the compounding of multiple data sets, allowed the creation of high quality angiograms free from eye motion. The quality of the *in vivo* human retinal angiograms presented in this paper comes close to the quality that, in the past, was reserved for *in vitro* experiments [13] and experiments on anesthetized animals [12]. Although Doppler noise shadows of the retinal vasculature still obscure parts of underlying vasculature, for the first time the mesh-like network of the choriocapillaris was imaged *in vivo* with phase-resolved OCT angiography. The smallest reported inter-capillary distances for the choriocapillaris are on the order of 5 µm [41] and require adaptive optics for clear observation. In this study the larger choriocapillaris pores with diameters ranging from 20 to 30 µm were visualized without adaptive optics. Phase-resolved OCT angiography therefore shows the potential to study (parts of) the choriocapillaris with standard OCT sample-arm hardware without the use of adaptive optics.

Real-time TSLO eye tracking is expected to be very advantageous for phase-resolved OCT angiography in clinical investigations in patients with compromised fixation due to disease, age or trauma.

6. Conclusions

In conclusion, we have demonstrated real-time tracking SLO for eye motion correction in phase-resolved OCT angiography of the retina and the choroid.

Tracking SLO provides an improved spot stability on the retina, corrects eye drift and prevents discontinuity artifacts from microsaccades in angiograms. This enabled the accurate compounding of several data sets from the same location to create high-quality eye motion artifact-free angiograms of the retina, the choroid, and the choriocapillaris.

Phase-resolved OCT angiography combined with real-time eye tracking is very promising for clinical investigations on vascular pathology in patients.

Appendix A: Laser safety considerations

In this appendix the laser safety considerations are described to indicate that the combined OFDI-TSLO setup was safe in its use during the experiments described in this paper.

A.1. Accidental exposure to stationary spots

The optical powers used by the combined OFDI-TSLO setup were 0.5 mW at 840 nm (TSLO) and 1.5 mW at 1050 nm (OFDI). According to ANSI 2007 [42] the recommended maximum permissible exposure (MPE) levels for exposure to a stationary spot on the retina for longer than 10 seconds are 0.733 mW for 840 nm and 1.93 mW for 1050 nm. These MPE levels are higher than the powers of the individual beams and therefore the used optical powers will not pose a hazard in the event that the lateral scanning stops simultaneously for both lasers. Moreover, this event is unlikely since it requires a double failure (failure of both scanning systems). The probability that both beams become superimposed during this event is even significantly smaller than the double failure event, since the lateral scanning of both lasers is independent and unsynchronized from each other, and happens over different field sizes and with different frame rates (see Subsection A.2). This special case is therefore negligible.

A.2. Exposure during lateral scanning

During normal imaging both beams are scanned laterally over the retina and their energy is distributed across a large retinal region, lowering the potential retinal irradiance at any location and increasing the MPE. Considering exposure times of 300 seconds, which is much longer than the actual exposure time at any given location, and applying a strict interpretation of ANSI rule 3 for pulsed line segment exposure [43] the MPEs for both beams are calculated

depending on their lateral field sizes, frame rates, and exposure duty cycles as given in Table 1.

Table 1. MPE levels at the cornea for the TSLO and the OFDI systems during (volume) scanning[a]

System	Field size (deg)	Frame rate (Hz)	Duty cycle (%)	MPE (mW @ cornea)
TSLO	4×4	30	40	1.1
OFDI	6.7×6.7	0.16	100	9.29

[a]The frame rate is the frequency with which the (retinal) field size is scanned over time. The duty cycle is the percentage of the lateral scanning for which the laser light is switched on.

The exposure to the laser light when the beams overlap is considered safe when the sum of the powers of each source divided by its MPE is not greater than 1 [42], which is the case when the two systems are scanning simultaneously:

$$\frac{power_{TSLO}}{MPE_{TSLO}} + \frac{power_{OFDI}}{MPE_{OFDI}} = \frac{0.5\,\text{mW}}{1.1\,\text{mW}} + \frac{1.5\,\text{mW}}{9.23\,\text{mW}} = 0.62. \qquad (A.1)$$

A.3. Exposure during OFDI retinal spot stability measurements

In Subsection 3.1 the retinal spot stability was evaluated using a stationary OFDI beam. The exposure conditions for the TSLO were equal as described in Table 1. In this experiment the stationary OFDI beam was always placed outside of the TSLO field as a safety precaution. The exposure time, which included the time to engage the eye tracking and perform the OFDI data recording, was never longer than 1 second. For a 1 second (accidental) exposure to a stationary beam, the MPE for 1050 nm light is 3.47 mW [42]. In the accidental case that the stationary OFDI beam overlapped with the TSLO field during the experiment the sum of the powers divided by their MPEs is not greater than 1 and the exposure is considered safe:

$$\frac{power_{TSLO}}{MPE_{TSLO}} + \frac{power_{OFDI}}{MPE_{OFDI}} = \frac{0.5\,\text{mW}}{1.1\,\text{mW}} + \frac{1.5\,\text{mW}}{3.47\,\text{mW}} = 0.89. \qquad (A.2)$$

Acknowledgments